ELSEVIER

Solid State Ionics 146 (2002) 163–174

SOLID STATE IONICS

www.elsevier.com/locate/ssi

Composites of $Ce_{0.8}Gd_{0.2}O_{1.9}$ and $Gd_{0.7}Ca_{0.3}CoO_{3-\delta}$ as oxygen permeable membranes for exhaust gas sensors

U. Nigge [a], H.-D. Wiemhöfer [a,*], E.W.J. Römer [b], H.J.M. Bouwmeester [b], T.R. Schulte [c]

[a] *Institute for Inorganic Chemistry and SFB 458, University of Münster, Münster, Germany*
[b] *Laboratory of Inorganic Materials Science, Department of Chemical Technology, University of Twente, Enschede, The Netherlands*
[c] *Corporate Research and Development, Robert Bosch GmbH, Stuttgart, Germany*

Received 14 February 2001; received in revised form 4 September 2001; accepted 4 September 2001

Abstract

The transport and catalytic properties of mixed conducting composites prepared from $Gd_{0.7}Ca_{0.3}CoO_{3-\delta}$ (GCC) and $Ce_{0.8}Gd_{0.2}O_{1.9}$ (CGO) were determined. In total, three compositions with 43, 60 and 75 vol.% CGO have been prepared. The composites have potential applications as oxygen permeable membrane in an amperometric sensor for NO_x detection in exhaust gases.

At all compositions, three different phases were found in the annealed composite as a result of solid state reactions during annealing. The gadolinium content of the CGO phase was increased. The GCC was transformed into a phase with K_2NiF_4-structure and an additional CoO phase appeared.

Electron conductivities were determined in the range 100 to 750 °C. The oxygen ion conductivities were measured by a microelectrode technique between 650 and 750 °C. Permeation measurements were carried out between 850 and 1000 °C. Effective ionic conductivities were calculated from the permeation results. The latter agreed well with the microelectrode data extrapolated to higher temperatures. The composition dependence of the conductivities was explainable by a statistical percolation model.

The investigated composites exhibit good oxygen ion conductivities. Typical ionic conductivity values for a composite with 75 vol.% CGO increased from 4×10^{-4} $(\Omega\ \mathrm{cm})^{-1}$ at 650 °C to 4.2×10^{-2} $(\Omega\ \mathrm{cm})^{-1}$ at 1000 °C.

The heterogeneous catalysis of surface gas reactions was tested by exposing powdered samples to various gaseous mixtures with O_2, N_2, CO, CO_2, H_2O, SO_2 and propene at temperatures up to 800 °C. No conversion of NO to oxygen and nitrogen as well as no extensive formation of N_2O was detected. It is concluded that the composite membranes are suitable for the intended applications.

Keywords: Oxygen ion conductivity; Oxygen permeation; Composite membrane; Catalytic activity; Ceria; $Ce_{0.8}Gd_{0.2}O_{1.9}$; $Gd_{0.7}Ca_{0.3}CoO_3$; Mixed conductor; Ceria; NO_x sensor

1. Introduction

Electrochemical gas sensors for a simultaneous analysis of NO_x and O_2 in exhaust gas mixtures require an electrode with high selectivity towards

* Corresponding author. Tel.: +49-251-83-33115; fax: +49-251-83-33193.
E-mail address: hdw@uni-muenster.de (H.-D. Wiemhöfer).

0167-2738/02/$ - see front matter
PII: S0167-2738(01)00984-5

oxygen in order to distinguish it from the one order of magnitude lower NO_x concentration. One way to achieve this is to cover the oxygen reducing electrode by a mixed ionic and electronic conducting (MIEC) membrane that is permeable to oxygen, but at the same time does not catalyse the decomposition of NO_x or reaction of O_2 with other gases at its surface.

This paper describes the results of our efforts to find a composite material with high chemical stability under exhaust gas conditions which meets the demands of efficient oxygen permeation combined with a minimised interference by NO decomposition or reaction with other gas components at the surface.

$Ce_{0.8}Gd_{0.2}O_2$ was chosen for the composite $Ce_{0.8}Gd_{0.2}O_2/Gd_{0.7}Ca_{0.3}CoO_3$ system as the oxygen ion conducting phase, because doped ceria shows high stability and good oxygen ion conductivity [1–5]. The use of $Gd_{0.7}Ca_{0.3}CoO_3$, on the other hand, ensures electronic conductivity of the mixed conducting composite. In this article, we will use the following abbreviations for the starting materials: CGO = $Ce_{0.8}Gd_{0.2}O_{1.9}$, GCC = $Gd_{0.7}Ca_{0.3}CoO_3$. An important aspect of using GCC is its low catalytic activity towards decomposition of NO [6]. For the combination CGO/GCC, we therefore expect a membrane material with high selectivity towards oxygen and a minimised interference with NO_x. Gadolinium, as a common component of both phases, further limits the number of possible reaction products during sintering of the membranes.

2. Experimental

2.1. Preparation

The composite membranes were prepared in several steps: the starting materials CGO and GCC were obtained by calcining and sintering of suitable precursor materials. The resulting powders were either intimately mixed in a mortar or ball-milled on a rollerbench using zirconia balls and ethanol as milling media. Finally, the powders were pressed to pellets and sintered. Three compositions were prepared with molar ratios GCC/CGO of 1:1, 1:2 and 1:4. These compositions correspond to 43, 60 and 75 vol.% CGO in the initial starting mixture.

Two methods, EDTA and spray-freezing/freeze-drying, were used to prepare the precursors. Emphasis was laid on low reaction temperatures for the final formation of the oxides as well as on small particle size and good dispersion in the final composite.

In the *EDTA-route*, solutions of the metal ions for each compound were mixed in stoichiometric proportions with EDTA. Excess water was removed from the solution of the metal complexes by evaporation on a hot plate until a gel like product was formed. The product was decomposed in a furnace at 400 °C and the resulting powder was subsequently calcined in air at 950 °C for 10 h. A good complexation of the ions is necessary in order to prevent agglomeration or a premature precipitation [7].

In the second method, *spray-freezing/freeze-drying* [8,9], aqueous solutions of the desired metals were prepared by dissolving the corresponding acetates or nitrates controlling the correct stoichiometric composition by complexometric titration. The aqueous solutions were sprayed into liquid nitrogen (spray-freezing step). Subsequently, the finely divided particles of the frozen solution were freeze-dried under vacuum. Finally, the resulting powder was decomposed and calcined in air in the same way as in the EDTA route.

For ionic conductivity measurements, pellets with various GCC/CGO contents were uni-axially pressed at 560 MPa and subsequently sintered in air at 1250 °C for 16 h. The relative density was $\rho^{rel} \approx 94\%$ ($\pm 2\%$). For permeation measurements the powders were uni-axially pressed to pellets at 10 MPa and, subsequently, isostatically pressed at 400 MPa. The resulting samples were sintered at 1200 °C for 10 h. After sintering, the relative density was $\rho^{rel} \approx 96\%$ ($\pm 2\%$). Prior to the ionic conductivity measurements, the pellets were polished extensively with 1 μm diamond paste to ensure a minimised surface roughness for the polarisation measurements. The samples for permeation were polished with 1000 MESH SiC.

2.2. Measurement of the electronic conductivity

The van der Pauw method was applied to cylindrical pellets of the composite materials [10]. The pellets had 6 mm diameter (d) and 3 mm height. Four

small area CrNi contact lines were sputtered symmetrically around the pellets (thickness 500 Å). The CrNi layers were non-porous. If oxygen exchange occurs at the CrNi contacts, the results would yield the total conductivity of ions and electrons. However, in the low temperature region below 750 °C, the CrNi contacts showed no catalytic activity towards the oxygen electrode reaction and therefore were blocking for the oxygen ions. Accordingly, the oxygen ion current in the sample pellets was suppressed and the measured conductivities corresponded to the electronic conductivities.

The electronic conductivities were evaluated from the measured DC currents and voltages in the temperature range from 100 to 750 °C using:

$$\sigma_e = -\frac{2\ln 2}{\pi d\left[\frac{U_{12}}{I_{34}} + \frac{U_{23}}{I_{14}}\right]} \quad (1)$$

where the four peripheral contacts are numbered subsequently from 1 to 4, e.g. I_{34} means the current via the neighbouring contacts 3 and 4.

2.3. Measurement of the oxygen ion conductivity

The oxygen ion conductivity was determined from steady state current–voltage curves at electron blocking microcontacts according to the Hebb–Wagner technique. Yttria-stabilised zirconia (YSZ, 20 mol% Y) was used for the microcontact in the form of ceramic needles. Theory and experimental details of the microelectrode technique have been described at length elsewhere [9,11–13]. Thus, we only present the experimental parameters and equations used for the evaluation of current–voltage curves.

The electrochemical cell is schematically shown in Fig. 1. The contact radius a of the microcontact ranged between 70 and 110 ± 10 μm. The measurements were performed inside a shielded furnace in a temperature range between 650 and 750 °C. The current was monitored during slow triangular voltage sweeps with a stepwise voltage change (10 mV steps) at a rate of 0.25–0.1 mV/s or lower. The voltage between the microelectrode and the reference contact (i.e. the Pt paste at the YSZ needle in air) varied between +0.080 and −0.150 V. The maximum possible sweep velocity is limited by the oxygen diffusion rate in the mixed conducting membrane material around the microcontact after voltage changes. If the sweep rate is too fast, a large hysteresis is observed in the current–voltage curves. The time duration of a complete voltage sweep should be at least 10 times the diffusion time constant $a^2/2D$ (D—chemical diffusion coefficient of oxygen) in order to ensure nearly steady state conditions of the concentration profiles at the microelectrode and minimal hysteresis.

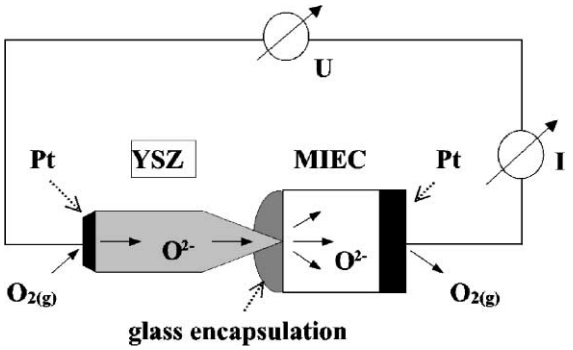

Fig. 1. Set-up for the measurement of the oxygen ion conduction based upon the use of microcontacts (YSZ = yttria stabilised zirconia).

Figs. 2 and 3 show typical current–voltage curves as a function of temperature. Fig. 2 demonstrates the necessity of a gas tight encapsulation of the sample surface around the microcontact. Compared to encapsulated samples, at a given potential the resulting current is 1.5 to 2 times larger if no encapsulation is applied, indicating that the surface oxygen electrode reaction is fast. This parallel electrode reaction results in a parasitic contribution to the oxygen ion conductivity, which leads to an overestimate of this conductivity. Therefore, in order to measure accurately, we have to exclude the electrode reaction by a careful glass encapsulation.

For the evaluation of oxygen ion conductivities as a function of oxygen partial pressure, the following basic equations were applied, which in principle correspond to the Hebb–Wagner model of polarisation at blocking electrodes [14–16].

Assuming a hemispherical contact surface at the microcontact, the local oxygen ion conductivity in

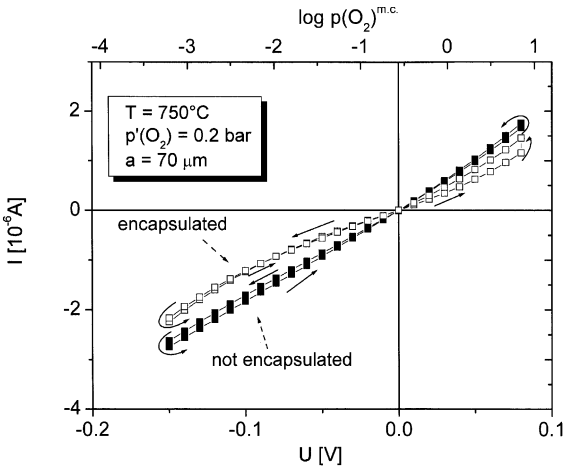

Fig. 2. Steady state $I-U$ curves at 750 °C for a GCC/CGO composite (43 vol.% CGO) contacted with a YSZ microcontact: demonstration of the difference between glass encapsulated and free microcontact. The surface exchange of oxygen with the surrounding gas phase leads to higher current due to the additional electronic current in the mixed conducting sample.

the sample at the microcontact is proportional to the slope of the steady state current–voltage curve:

$$\sigma_{O^{2-}}(p_{O_2}^{m.c.}) = \frac{1}{2\pi a}\frac{dI}{dU} \quad (2)$$

$p_{O_2}^{m.c.}$ represents the effective oxygen partial pressure at the interface between sample and microcontact which is determined by the cell voltage U in the steady state:

$$U = \frac{RT}{4F}\ln\frac{p_{O_2}^{m.c.}}{p'_{O_2}} \quad (3)$$

p'_{O_2} denotes the constant reference oxygen partial pressure at the counter electrode.

2.4. Measurement of oxygen permeation

The oxygen permeation of the composite materials was measured for three different CGO contents (43, 60 and 75 vol.%) in the temperature range 850–1000 °C. Disk samples with a diameter of 15 mm and a thickness of 1.5 mm were used. Prior to the measurements, the samples were polished with 1000 Mesh SiC. The membrane was subsequently sealed in a quartz reactor at 1100–1150 °C in air using Supremax glass rings (Schott Nederland). Air and high purity helium gas were used as feed and sweep gas on the two sides of the membrane disk, respectively. A Varian 3400 gas chromatograph was used to monitor the composition of the sweep. A detailed description of the set-up is given elsewhere [17]. The oxygen permeation flux was calculated from:

$$j_{O_2} = \frac{1}{G}\frac{I_V c_{O_2}^{perm}}{A} \quad (4)$$

in which I_V is the flow rate at the outlet of the reactor (m^3/s (STP)), $c_{O_2}^{perm}$ the oxygen concentration in the permeate stream (mol/m^3) and A the geometric surface area at the He-side of the membrane (m^2). G is a dimensionless factor of the order of one that corrects for the effect of non-axial diffusion. This non-axial diffusion is caused by the sealing into the reactor, which leads to different surface areas for the feed and permeate side of the membrane.

In order to compare the permeation rates with values of the oxygen ion conductivities, we derived oxygen ion conductivities from the permeation rates according to the following model. Ambipolar transport of oxygen in the form of oxygen ions and electrons through a MIEC membrane can be described using the Wagner theory. To simplify the notation, we define an ambipolar effective conduc-

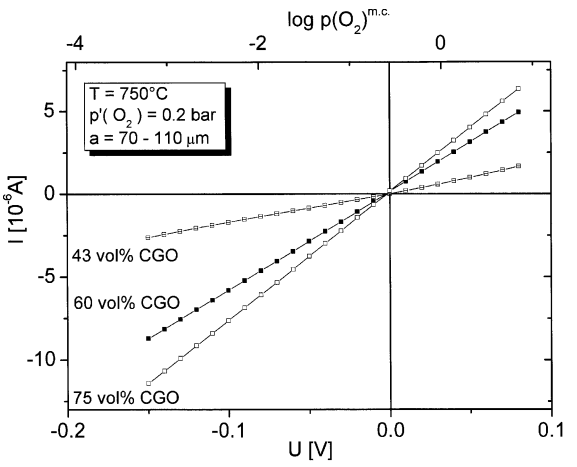

Fig. 3. Compositional dependence of the steady-state $I-U$ curves at 750 °C (glass encapsulated microcontact).

tivity σ_{amb}, which for a homogeneous membrane material is given by:

$$\sigma_{amb} = \frac{\sigma_{O^{2-}}\sigma_e}{\sigma_{O^{2-}} + \sigma_e} \quad (5)$$

where $\sigma_{O^{2-}}$ denotes the oxygen ion conductivity and σ_e the electronic conductivity (S/cm).

Assuming that surface exchange is fast compared to bulk diffusion and that the partial conductivities are independent of oxygen partial pressure, the oxygen flux can be expressed by [18]:

$$j_{O_2} = \frac{\sigma_{amb}RT}{4F^2L}\ln\frac{p_{O_2}^{air}}{p_{O_2}^{He}}. \quad (6)$$

Here, j_{O_2} is the oxygen flux in mol/(m^2 s), R the gas constant, T the absolute temperature in Kelvin, F the Faraday constant, L the thickness of the membrane in m, $p_{O_2}^{air}$ and $p_{O_2}^{He}$ are the oxygen partial pressures at the feed and permeate side of the membrane, respectively.

In the case of composite membranes consisting of separate phases with exclusive ionic or electronic conductivity, there is no locally coupled movement of electrons and ions, but a separate transport in distinctive phases. However, if an intimate mixture of the two phases exists, it is also possible to define an effective ambipolar conductivity to be applied in Eq. (6) under these circumstances [19]:

$$\sigma_{amb} = \frac{\varphi_{O^{2-}}\sigma_{O^{2-}}^{eff}\varphi_e\sigma_e^{eff}}{\varphi_{O^{2-}}\sigma_{O^{2-}}^{eff} + \varphi_e\sigma_e^{eff}}. \quad (7)$$

The superscript "eff" denotes a correction of the conductivity for geometrical effects (percolation) and $\varphi_{O^{2-}}$ and φ_e are the volume fractions of the oxygen ion conducting and the electron conducting phase, respectively.

2.5. Measurement of catalytic activities

Temperature programmed reaction (TPR) experiments were used to evaluate the catalytic activity of these materials. A powdered sample, with a BET-surface area of approximately 1.2 m^2/g, was placed inside a flow reactor consisting of a U-shaped quartz glass tube. Prior to use, the powders were annealed at 1200 °C for 12 h and ball milled (12 h) using zirconia balls on a roller bench.

Gas with a constant initial composition of O_2, NO, C_xH_y in N_2 was fed to the reactor with a constant flux of the order of 1000 cm^3 min^{-1}. Typical concentrations were 850–1000 ppm NO, 850–1000 ppm C_3H_6, 0–5% H_2O and 2% O_2 in N_2. Calibrated mass flow controllers were used to generate the required gas-mixture from high purity grade gases. The high flow rate was required by the analytical equipment. Nevertheless, with adequate powder volumes, catalytic effects occurring at the material surface in contact with the simulated exhaust gas mixture were easily detectable.

For each of the applied gas compositions, the reactor was continuously heated from 25 up to 950 °C with a rate of 5 °C min^{-1}. During the following cooling process, pure nitrogen was applied to guarantee the same initial conditions for the next run.

The gas composition was analysed before and after passage through the reactor tube. Because in the presence of oxygen the ratio NO/NO_2 cannot be held constant due to conversion of NO to NO_2 in the cooler parts of the system, only the total amount of $NO_x = NO + NO_2$ was determined using an equipment based on a chemoluminescence detector (Rosemount 951A). C_xH_y-components were detected using a FID analyser (Tesata FID 123). Carbon oxides were measured using a non-dispersive infrared analyser (NDIA, Uras 10E Hartmann and Braun). An electrochemical cell was used to measure the oxygen content in the gas.

To exclude any interference by catalytic effects of the reactor wall on the results, additional measurements without any powder load were carried out. No conversion of NO to oxygen and nitrogen or N_2O was detected within the chosen temperature range under these conditions.

2.6. SEM–EDX

SEM–EDX measurements were performed on the three samples, which were also used for the permeation rate experiments (CGO contents: 43, 60 and 75 mol%). The results served also as background information concerning the estimation of the percolation thresholds in the permeation measurements.

The samples were examined by back-scattered electron imaging using SEM (JEOL JSM5800) operating at 20 kV. The composition of the samples was

determined by SEM–EDX using a Hitachi S-800 Field Emission Microscope operating at 15 kV, which was coupled to a Kevex Delta Range EDX system for surface element analysis.

3. Results and discussion

3.1. Microstructure and phase distribution of the composites

An example of a SEM observation is given in Fig. 4 for the composite with 43 vol.% CGO in the starting mixture. To enhance the differences in phase composition, back scattered electrons were used. At least three different phases can be distinguished. A topographic surface scan revealed that the dark phases are situated somewhat beneath the surface.

The brightest phase in Fig. 4 (denoted as phase 1) contained mainly Ce and Gd (see Table 1a) and therefore corresponds to the oxygen ion conducting doped ceria phase. Semiquantitative analysis showed that almost equal concentrations of Ce and Gd are present which means that the Gd concentration increased significantly as compared to the 80% Ce and 20% Gd of the starting CGO material. The additional Gd must be attributed to a decomposition of the perovskite phase with initial composition $Gd_{0.7}Ca_{0.3}CoO_3$.

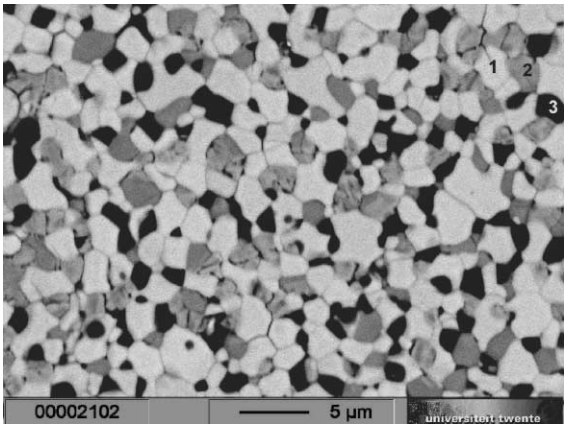

Fig. 4. SEM observation of the surface of a GCC/CGO composite with 43 vol.% CGO in the starting mixture (Magnification 5000 ×; composition of phases denoted as 1, 2, 3: see Table 1).

Table 1
Composition of the different phases detected in GCC/CGO composites

Element	1 (bright)	2 (grey)	3 (dark)	Intended	Overall
(a) 43 vol.% CGO					
Ce	53	–	–	27	26
Gd	43	37	–	30	30
Ca	2	30	–	10	11
Co	2	33	+	33	33
(b) 60 vol.% CGO					
Ce	65	5	2	40	38
Gd	32	30	1	28	27
Ca	1	33	2	8	8
Co	2	33	95	25	26
(c) 75 vol.% CGO					
Ce	63	6	3	53	46
Gd	33	29	3	25	25
Ca	1	31	13	5	7
Co	3	33	81	17	22

1 is the brightest phase, 3 the darkest (see the indicated phases denoted 1, 2, 3 in Fig. 4). Values in each column are given in mol% for the respective phase (1, 2, 3) in each composite.

Accordingly, the second phase (grey phase, denoted phase "2" in Fig. 4), although it contained all three cations of the starting material $Gd_{0.7}Ca_{0.3}CoO_3$, did not correspond to that intended composition. Indeed, it showed an increased Ca content and a considerably decreased Co content. The actual metal stoichiometry in the grey phase ("2" in Fig. 4) approaches a ratio near (Gd + Ca):(Co) = 2:1. This phase composition was found in all three investigated composites which gives a strong indication for the presence of a phase with K_2NiF_4 structure, which recently also was detected in membranes of initially single-phase GCC ($Gd_{0.7}Ca_{0.3}CoO_3$) after sintering [6,20]. Although the calcium content is slightly higher, quantitative EDX-analysis of the grey phase as given in Table 1a–c is consistent with that. In our previous study, GCC with a starting composition of $Gd_{0.7}Ca_{0.3}CoO_x$ was found to disintegrate during sintering in air into a three-phase mixture, i.e. $(Gd_{0.6}Ca_{0.4})_2CoO_x$ with K_2NiF_4 structure, which contained almost all of the original Ca, and two additional decomposition products, i.e. CoO and (in a minor amount) the perovskite $GdCoO_3$ [6]. Our composites, however, did not show a remaining $GdCoO_3$ phase. This may be explained by the

presence of ceria which dissolves additional Gd and thus enhances decomposition of $GdCoO_3$.

The third phase (denoted as phase 3 in Fig. 4) is CoO. An overview of the results of the EDX analysis of all investigated composite materials is given in Table 1a–c. The data from SEM–EDX clearly show, that a solid state reaction has occurred during sintering: A considerable amount of gadolinium is extracted from the initial GCC starting composition increasing the gadolinium content in the CGO phase. For instance, the following approximate reaction stoichiometry may explain the observed changes after sintering of a CGO/GCC mixture with 60 vol.% CGO corresponding to a molar ratio CGO/GCC of 2:1 [cf. Table 1b:

$$\begin{aligned}&\text{phase1} \approx \text{“}Ce_{0.65}Gd_{0.35}O_{2-\delta}\text{”},\\ &\text{phase2} \approx \text{“}(Gd_{0.5}Ca_{0.5})_2CoO_{4-\varepsilon}\text{”},\\ &\text{phase3} \approx \text{“CoO”}].\end{aligned}$$

$$2\ Ce_{0.8}Gd_{0.2}O_{1.9} + Gd_{0.7}Ca_{0.3}CoO_{3-\varepsilon} \rightarrow x\ \text{phase1} + y\ \text{phase2} + z\ \text{phase3} + w\ O_{2(g)}. \quad (8)$$

The stoichiometric coefficients x, y, z of the product phases in Eq. (8) are approximately $x=2.35$, $y=1.13$, $z=0.61$, if the conservation of mass is accounted for in the reaction and the analytical results of Table 1 are used. Only the result for the overall Ca content is higher than expected indicating local inhomogenities with respect to Ca. Accordingly, the percentage of the oxygen ion conducting phase in the composite is slightly larger than the intended concentration in the starting mixture.

The driving force of this reaction seems to be the instability of Co^{3+} at high temperature in the initial GCC (as well known from other cobaltates such as $La_{1-x}Ca_xCoO_{3-\varepsilon}$) and probably a higher stability of the K_2NiF_4 phase relative to that of the perovskite structure. As argued above, the loss of gadolinium in favour of the doped ceria phase may further increase the driving force towards decomposition yielding CoO as a third phase. Fig. 4 shows dark isolated CoO particles being always in contact with doped ceria particles.

The observed solid-state reactions are presumably diffusion limited and should depend on the sintering time as well as on the particle size and the degree of dispersion of the different phases. Therefore, it is explainable that the turnover of the reaction is reduced, if the powders are not milled before, i.e. larger regions with homogeneous composition occur. As can be seen in Fig. 5, omitting the milling step resulted in larger areas with Ce and Gd (bright areas) and areas consisting of several phases containing the metals Co, Gd, Ca (dark areas). In this case, the ratio between Ce and Gd in the bright phase of Fig. 5 (corresponding to “1” in Fig. 4) was closer to the molar ratio Ce:Gd = 80:20 of the CGO starting material and amounted to Ce:Gd = 68.2:31.8.

3.2. Transport of electrons and oxygen ions

Fig. 6 presents the Arrhenius plots of the electronic conductivity (van der Pauw method) as a function of the CGO content. The temperature dependence of pure (sintered) GCC and the two GCC rich mixtures corresponds to an average activation energy of 0.28 ± 0.02 eV. In general, the observed magnitudes and the temperature dependence are typical for a semiconducting compound.

The sample with initial 75 vol.% CGO shows a small slope at lower temperatures and a steeper one above 400 °C. The steeper slope indicates a transition to a predominating electron transport in the ceria derived phase comparable to pure ceria (lowest curve in Fig. 6). Data are clearly indicating that electronic conductivity is enhanced by addition of GCC as

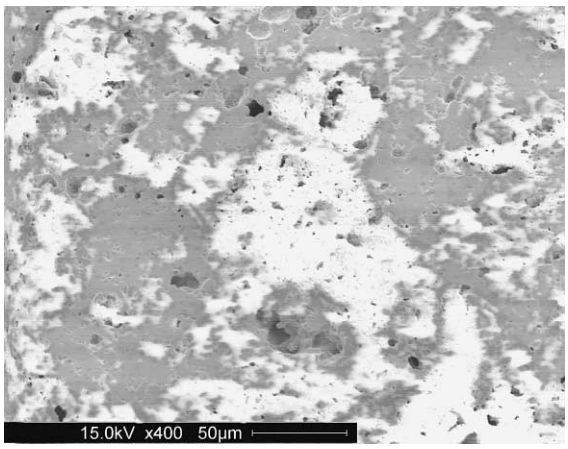

Fig. 5. SEM observation of a 43 vol.% GCC/CGO composite. Powders were not milled prior to pressing. Magnification 400 × .

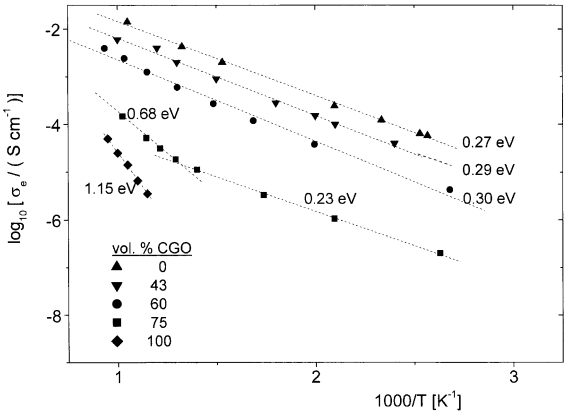

Fig. 6. Electronic conductivity of GCC/CGO as a function of the CGO content and the temperature in air.

electron conducting phase. We conclude that for samples with less than 75 vol.% CGO the electronic conductivity is dominated by electron transport in the GCC derived phases of the composites.

Fig. 7 shows the oxygen ion conductivities of the composites as a function of oxygen partial pressure at 750 °C measured with the microcontact technique. Table 2 lists the oxygen ion conductivities together with the activation energies for the temperature range 650 to 750 °C as obtained from microcontact measurements. As expected, the oxygen ion conductivity increases with increasing ceria content of the composite. Besides that the ionic conductivities of 60 and 75 vol.% CGO composites are independent of oxygen partial pressure. On the other hand, comparable to pure GCC, the values of the sample with 43 vol.% ceria are slightly dependent on the oxygen partial pressure. We assume that the oxygen ions are predominantly transported along the ceria rich particles in the samples. A high ceria content and a good dispersion of the particles (see Fig. 4) guarantee a sufficient number of continuous paths. However, no continuous paths of the ceria phase are present in the sample with 43 vol.% CGO. Therefore, it can be stated that this composition is not percolative with regard to the ion conducting phase. The slight partial pressure dependence of this composite, as illustrated in Fig. 7, suggests that oxygen ion movement is limited by the passage through GCC derived particles.

The data on oxygen ion transport were completed towards higher temperatures (850–1000 °C) by permeation measurements. In Table 3, the results of these measurements are presented. Table 4 lists the effective mean oxygen ion conductivities as calculated from the measured permeation data using Eq. (6).

An Arrhenius plot of the oxygen ion conductivity data of both permeation and microcontact measurements is given in Fig. 8. The data for the three composites match reasonably well. However, for pure GCC a large gap between the results from permeation and microcontact measurements is apparent. It seems likely that the slow surface kinetics of oxygen exchange for GCC is responsible for this difference, because the microcontact technique involves direct transfer of oxygen ions which is less hindered than the oxygen reduction occurring in the permeation experiment.

At temperatures below 800 °C, the activation energy of the oxygen conductivity of the composite with 43 vol.% CGO is comparable to that of pure GCC (see Fig. 8). This gives additional support for the assumption that oxygen ion transport in the 43 vol.% sample is slowed down due to the low ion conductivity of GCC and the lack of continuous ion conducting CGO paths. Furthermore, the temperature dependence of the composites with 60% and 75% CGO is very similar to that of pure CGO.

The obtained electronic and ionic conductivity data as a function of the CGO content were compared with a recently published percolation model for

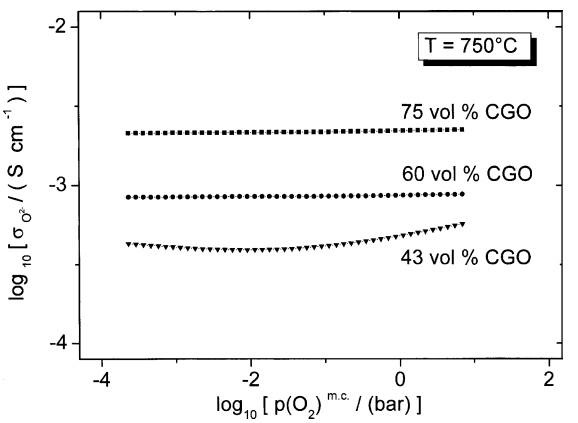

Fig. 7. Double logarithmic plot of the oxygen ion conductivity versus the oxygen partial pressure at a temperature of 750 °C for the three investigated composites (results from the microcontact technique).

Table 2
Oxygen ion conductivities of GCC/CGO-composites as a function of initial CGO content and temperature as derived from the microelectrode technique

x [vol.% CGO] →	0 (pure GCC)	43%	60%	75%	100% (pure CGO)
T [K]	$\sigma_{O^{2-}}$ [S/cm]				
650	3.2×10^{-6}	1.9×10^{-5}	2.6×10^{-4}	6.2×10^{-4}	8.4×10^{-3}
700	9.0×10^{-6}	9.0×10^{-5}	5.5×10^{-4}	1.2×10^{-3}	1.3×10^{-2}
750	8.0×10^{-5}	4.3×10^{-4}	1.0×10^{-3}	2.2×10^{-3}	2.0×10^{-2}
E_A [eV] →	1.9	1.7	1.1	1.0	0.9

The last row shows the average activation energies (± 0.1 eV) calculated from the temperature dependence of the ionic conductivities at a constant partial pressure of 0.209 bar (i.e. in air).

composites consisting of a pure ionic and a pure electronic conductor [21]. Although in our composites there are three instead of two phases, the basic behaviour should be comparable, because we have a composite of electronically and ionically conducting particles which is the basic assumption of the applied model [21]. The phases 2 and 3 in Table 1 are both electron conducting. For a composite with statistical distribution of electronically and ionically conducting particles, the total effective ionic and electronic conductivities each obey the following dependence on the volume fraction:

$$\sigma_k = \frac{1}{4}\left[E_a(\varphi_1) + \sqrt{E_a^2(\varphi_1) + E_b}\right]$$

(suffix k stands for e^- or O^{2-}) (9)

with the following definition:

$$E_a(\varphi_1) = 3[\varphi_1\sigma_{10} + (1-\varphi_1)\sigma_{20}] - (\sigma_{10} + \sigma_{20})$$
$$E_b = 8\sigma_{10}\sigma_{20}$$
$$\varphi_1 = \frac{V_1}{V_1+V_2}, \quad \varphi_2 = 1 - \varphi_1 \qquad (10a-c)$$

1 and 2 denote the electronically and ionically conducting phases in the composite and σ_{10} and σ_{20} denote either the ionic of the electronic conductivities of the respective pure phases.

Fig. 9 shows the experimental data for electronic and oxygen ion conductivity as a function of composition. In addition, two fitting curves are plotted. The two curves were fitted to the electronic and ionic conductivities of the three composites. The experimental values for the pure CGO and GCC do not fit well. This can be explained by the considerable changes in composition (and crystal structure of GCC) during annealing of the composites. The considerable increase of the Gd concentration in the CGO phase (cf. Table 1) after the annealing step causes a decrease of the oxygen ion conductivity as the initial composition $Ce_{0.8}Gd_{0.2}O_{1.9}$ corresponds to a maximum oxygen ion conductivity for Gd doped ceria [22,23]. Therefore, the oxygen ion conductivity of pure CGO is expectedly higher than predicted by the fit in Fig. 9. Within the applied percolation model, the value for the oxygen ion conductivity of pure GCC does not influence the fit to the three conductivity values of the composites because they lie above the percolation threshold. Within the limits of accuracy, the above interpretation gives a consistent picture for the composites. One concludes that

Table 3
Measured oxygen permeation rates of GCC/CGO composites as a function of temperature and composition

x [vol.% CGO]	$j(O_2)$ [mol/(cm^2 s)]			
	1000 °C	950 °C	900 °C	850 °C
0	8.76×10^{-10}	2.79×10^{-10}	5.26×10^{-11}	3.60×10^{-11}
43	4.04×10^{-8}	2.40×10^{-8}	1.44×10^{-8}	8.31×10^{-9}
60	3.79×10^{-8}	2.29×10^{-8}	1.34×10^{-8}	7.38×10^{-9}
75	8.33×10^{-8}	5.94×10^{-8}	3.74×10^{-8}	2.00×10^{-8}

Table 4
Effective oxygen ion conductivities as calculated from the permeation rates of Table 2 using Eq. (6)

x [vol.% CGO]	$\sigma^{eff}_{amb} \approx \sigma^{eff}_{O^{2-}}$ [S/cm]			
	1000 °C	950 °C	900 °C	850 °C
0	1.50×10^{-4}	4.81×10^{-5}	5.26×10^{-6}	6.59×10^{-6}
43	1.76×10^{-2}	1.10×10^{-2}	6.85×10^{-3}	4.12×10^{-3}
60	1.62×10^{-2}	1.02×10^{-2}	6.23×10^{-3}	3.58×10^{-3}
75	4.17×10^{-2}	3.10×10^{-2}	2.04×10^{-2}	1.14×10^{-2}

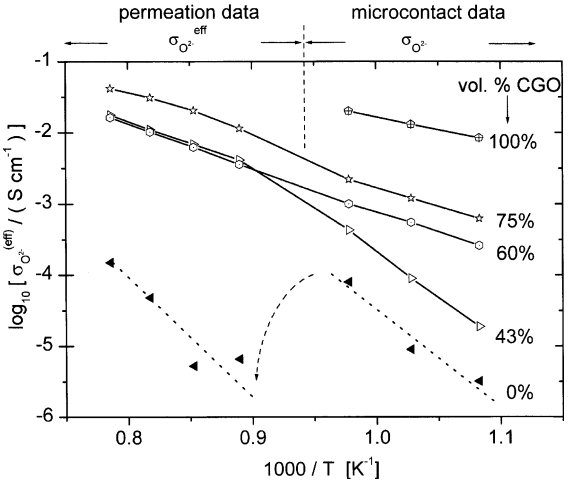

Fig. 8. Logarithm of the oxygen ion conductivities of the composite materials as obtained from permeation measurements ($T>800$ °C) and microcontact measurements ($T<800$ °C, oxygen partial pressure of 0.209 bar) as a function of inverse temperature for the three investigated composites and the pure single-phase materials.

the best compositions for the application as oxygen permeable membrane are those in the range 60 to 75 vol.% CGO.

3.3. Catalytic properties with regard to exhaust gases

The catalytic activity was analysed in non-equilibrium gas mixtures simulating the exhaust gas composition of Diesel engines. The aim was to get a mixed conducting membrane material that shows no or minimal catalytic activity towards NO reduction. The influence of surface oxygen vacancies of the mixed conducting composite on the promotion of the catalytic NO decomposition taking place on the composite material can be described by the following reaction steps [24]:

$$2\ e^- + NO_{(ad)} + V_O^{\bullet\bullet} \Rightarrow N_{(ad)} + O_O \quad (11)$$

$$N_{(ad)} + N_{(ad)} \Rightarrow N_{2(g)} \quad (12)$$

$$N_{(ad)} + NO_{(ad)} \Rightarrow N_2O_{(ad)} \quad (13)$$

$$2\ e^- + N_2O_{(ad)} + V_O^{\bullet\bullet} \Rightarrow N_{2(g)} + O_O. \quad (14)$$

The reaction scheme shown above includes the formation of N_2O. If no N_2O is detected, the following simpler reaction scheme applies for the decomposition of NO:

$$2\ e^- + NO_{(ad)} + V_O^{\bullet\bullet} \Rightarrow (NO^- - V_O^{\bullet}) \quad (15)$$

$$2\ (NO^- - V_O^{\bullet}) \Rightarrow N_{2(g)} + 2\ (O^- - V_O^{\bullet}) \quad (16)$$

$$(O^- - V_O^{\bullet}) \Rightarrow 2\ e^- + \frac{1}{2} O_{2(g)} + V_O^{\bullet\bullet}. \quad (17)$$

White et al. [25] reported conversion rates up to 72% using a flow of 1% NO in He at 800 °C over a series of different perovskites. According to their data, perovskites containing Co^{3+} on the B lattice-site, in general, show high activity towards NO decomposition.

However, as can be seen from Fig. 10, if an air-sintered-powdered sample (43 vol.% CGO) is exposed to 1000 ppm NO in N_2 no reduction of NO could be detected in the observed temperature range.

CO coming from the partial oxidation of hydrocarbon fuels is an important active reductant in the exhaust gases of internal combustion engines. Therefore, special attention has to be paid to its influence on the nitrogen oxide conversion, which may further influence the surface activity of the composite. Therefore, in a second experiment, 950 ppm propene

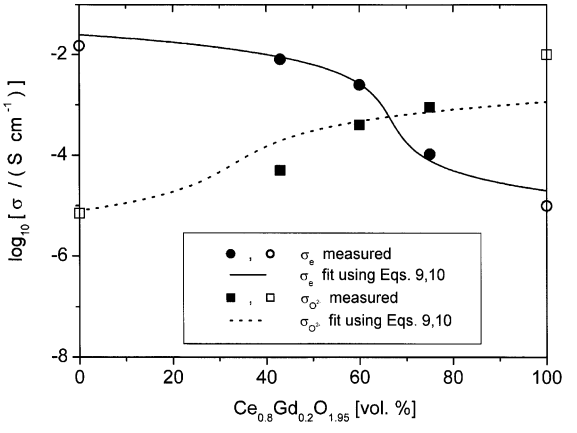

Fig. 9. Electron and oxide ion conductivities in the composite material GCC/CGO as a function of the composition at 650 °C: experimental results and fit according to the percolation model Eqs. (9) and (10a–c) [21]. Note that the phases in the composites have different compositions as compared to the pure single-phases CGO and GCC. The results on pure CGO and GCC (empty symbols) are therefore shown only for comparison with the composites (filled symbols).

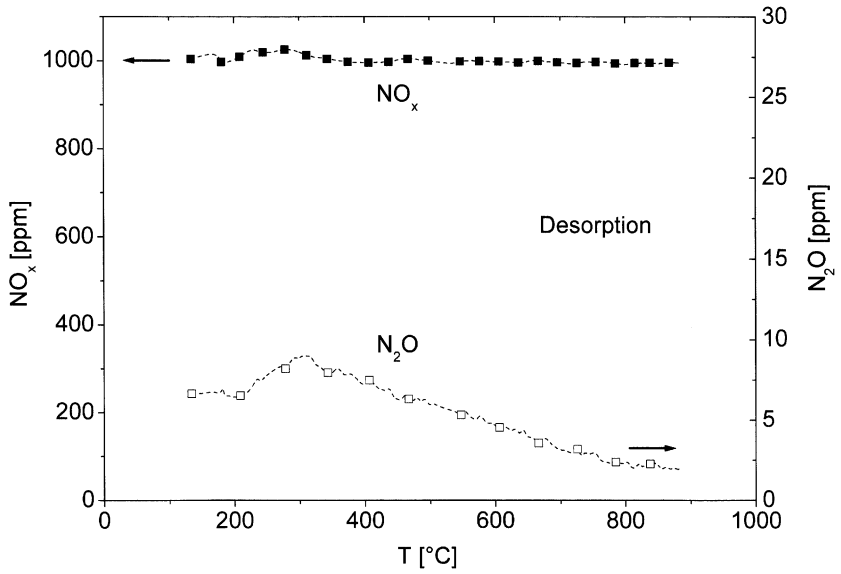

Fig. 10. Temperature dependence of NO_x and N_2O content in the measuring gas after passing over the GCC/CGO-sample (43 vol.% CGO; initial concentration of the gas: 1000 ppm NO in N_2).

were applied as a typical hydrocarbon together with 3 vol.% O_2 in the simulated exhaust gas mixture.

In spite of the presence of reducing agents, no indication for a reduction of nitrous oxide was observed below 800 °C. According to the experimental results presented in Fig. 11, the oxidation of the propene occurs in the presence of an excess of oxygen without any cross interference with the nitrous oxide concentration. Above 800 °C, only moderate decomposition of the nitrous oxide was observed. The presence of oxygen seems to inhibit any reduction of adsorbed NO at the composite surface.

If the initial oxygen partial pressure is increased, the onset of the propene oxidation shifts to lower temperatures. The high turnover rates for the oxidation of hydrocarbons and CO are not exceptional and well known for many perovskites based on La, Sr, Co or Mn [26,27]. Like in Fig. 10, a small increase in N_2O concentration shows that the surface of the composite material is interacting with the NO to a

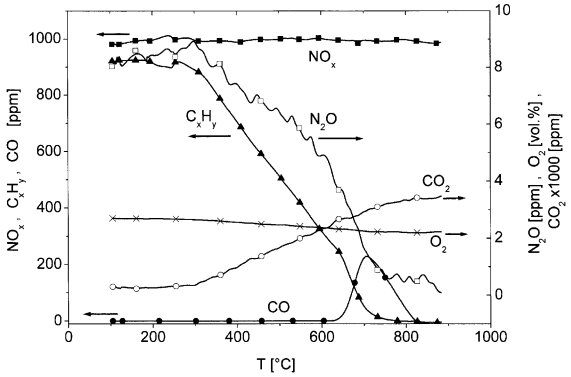

Fig. 11. Temperature dependence of the resulting gas concentration of NO_x, C_xH_y, CO_2, CO, N_2O and O_2 in the measuring gas after passing over the GCC/CGO-sample (43 vol.% CGO; initial concentration of the gas: 1000 ppm NO + 950 ppm C_3H_6 + 3% O_2 in N_2).

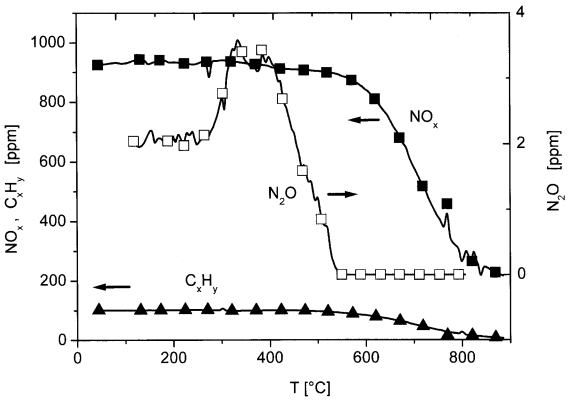

Fig. 12. Temperature dependence of the resulting content of NO_x, C_xH_y, and N_2O in the measuring gas after passing over the GCC/CGO-sample. (43 vol.% CGO; initial concentration of the gas: 950 ppm NO + 100 ppm C_3H_6 in N_2).

minor degree. However, an increasing concentration and oxidation rate of hydrocarbons at the composite surface clearly increases the reduction of N_2O (see Fig. 11). Therefore, one can expect that strongly reducing conditions, i.e. high concentrations of hydrocarbons in the exhaust gas, lead to an accelerated reduction of NO at the composite surface. This is indeed the result as seen in Fig. 12 where the oxygen content of the gas mixture was reduced to zero. A similar behaviour was found for pure $Gd_{0.7}Ca_{0.3}CoO_3$ itself [24].

4. Conclusion

The investigated GCC/CGO are interesting oxygen permeation membrane materials with high permeation rates and favourable surface kinetics for oxygen exchange. Although the annealing of the membranes during preparation leads to large changes in the type and composition of the contained phases with regard to their initial state, the membrane has attractive properties. Besides the good permeation rates of oxygen, the selectivity towards oxygen in the presence of NO_x is a property of interest for sensor applications in exhaust gas sensors. On the other hand, the results of the catalytic experiments clearly limit an application of the composite GCC/CGO as oxygen selective membranes only in lean oxidising exhaust gas mixtures.

References

[1] H.L. Tuller, Solid State Ionics 52 (1992) 135.
[2] R.T. Dirstine, R.N. Blumenthal, T.F. Kuech, J. Electrochem. Soc. 126 (1979) 264.
[3] N. Inaba, H. Tagawa, Solid State Ionics 83 (1996) 1.
[4] J.A. Lane, J.A. Kilner, Solid State Ionics 136 (2000) 927.
[5] E. Ruiz-Trejo, J.D. Sirman, Yu.M. Baikov, J.A. Kilner, Solid State Ionics 113 (1998) 565.
[6] E.W.J. Römer, U. Nigge, T.R. Schulte, H.-D. Wiemhöfer, H.J.M. Bouwmeester, Solid State Ionics 140 (2001) 97.
[7] R.H.E. van Doorn, H. Kruidhof, A. Nijmeijer, L. Winnubst, A.J. Burggraaf, J. Mater. Chem. 8 (9) (1998) 2109.
[8] S. Lübke, H.-D. Wiemhöfer, Solid State Ionics 117 (1999) 229.
[9] W. Zipprich, S. Waschilewski, F. Rocholl, H.-D. Wiemhöfer, Solid State Ionics 101–103 (1997) 1015.
[10] L.J. van der Pauw, Philips Res. Rep. 13 (1985) 1.
[11] H.-D. Wiemhöfer, Ber. Bunsen-Ges. Phys. Chem. 97 (1993) 461.
[12] H.-D. Wiemhöfer, F. Rocholl, W. Zipprich, T. Hauber, G. Reinhardt, Diffusion and Defect Forum, vol. 143–147, Scitec Publ., Uetikon-Zuerich, 1997, p. 1701.
[13] W. Zipprich, H.-D. Wiemhöfer, Solid State Ionics 135 (2000) 699.
[14] M.H. Hebb, J. Chem. Phys. 20 (1952) 185.
[15] C. Wagner, Proc. 7th Meeting Int. Committee of Electrochemical Thermodynamics and Kinetics, Lindau 1955, Butterworths, London, 1957, p. 361.
[16] I. Yokota, Jpn. J. Appl. Phys. 1 (1962) 144.
[17] J.E. ten Elshof, H.J.M. Bouwmeester, H. Verweij, Solid State Ionics 81 (1995) 97.
[18] H.J.M. Bouwmeester, A.J. Burggraaf, in: P.J. Gellings, H.J.M. Bouwmeester (Eds.), The CRC Handbook of Solid State Electrochemistry, CRC Press, Boca Raton, 1997, p. 481.
[19] C.S. Chen, Thesis, University of Twente, Enschede (1994).
[20] E.W.J. Römer, Thesis, University of Twente, Enschede (2001).
[21] Z. Wu, M. Liu, Solid State Ionics 93 (1997) 65.
[22] R.G. Anderson, A.S. Nowick, Solid State Ionics 5 (1981) 547.
[23] G.B. Balacs, R.S. Glass, Solid State Ionics 76 (1995) 155.
[24] T. Schulte, Dissertation, RWTH Aachen (2000).
[25] J. White, J. Burt, R.L. Cook, A.F Sammells, U.S. Department of Commerce, NTIS, Final Report PB92-164375 (1992).
[26] P.K. Gallagher, D.W. Johnson Jr., F. Schrey, Mater. Res. Bull. 9 (1974) 1345.
[27] P. Arnoldy, J.A. Moulijn, J. Catal. 93 (1985) 38.